This is a preprint, the final version is subject to change, of the American Mineralogist (MSA)
Cite as Authors (Year) Title. American Mineralogist, in press.
(DOI will not work until issue is live.) DOI: http://dx.doi.org/10.2138/am-2016-5509

REVISION 1

A story of olivine from the McIvor Hill complex (Tasmania, Australia): clues to the origin of the Avebury metasomatic Ni sulfide deposit

VADIM S. KAMENETSKY[1*], ALEXEY V. LYGIN[1], JEFF G. FOSTER[1], SEBASTIEN MEFFRE[1], ROLAND MAAS[2], MAYA B. KAMENETSKY[1], KARSTEN GOEMANN[3] and STEVE W. BERESFORD[4]

[1]School of Physical Sciences and CODES, University of Tasmania, Hobart, TAS 7001, Australia

[2]School of Earth Sciences, University of Melbourne, Parkville, VIC 3010, Australia

[3]Central Science Laboratory, University of Tasmania, Hobart, TAS 7001, Australia

[4]First Quantum Minerals, West Perth, WA 6005, Australia

[*]*Corresponding author, email Dima.Kamenetsky@utas.edu.au*

ABSTRACT

Magmatic differentiation and/or assimilation and related segregation of immiscible sulfide liquid are generally believed to be critical processes in the formation of the majority of orthomagmatic Ni sulfide deposits. In recent years, a new class of Ni sulfide deposits formed by metasomatic and/or hydrothermal modification of peridotites has been recognized. The serpentinite-hosted Avebury Ni sulfide deposit (Tasmania, Australia), the largest known non-magmatic deposit, provides an unprecedented opportunity to understand sources of metals and fluids responsible for this style of economic mineralization. Our study shows that serpentinization of the Ni-bearing olivine in the Cambrian peridotites of the McIvor Hill complex was followed by metasomatic transformation assisted by heat and fluids supplied by the nearby Late Devonian granite intrusion. The role of the above in the formation of an economic concentration of Ni sulfides is supported by 1) abundant Ni-Fe alloys and sulfides associated

with serpentinization of peridotitic olivine, 2) metasomatic olivine containing inclusions of serpentine and metalliferous brines and 3) the Late Devonian age of the Ni sulfide deposit. The Avebury metasomatic olivine is Ni-depleted and enriched in Mn relative to olivine of similar Fo content in nearby unmineralized peridotites, and to olivine in subduction-related mafic magmas generally. The unusual minor element chemistry of olivine is matched by a unique set of olivine-hosted multiphase inclusions composed of fibrous Mg-silicates and a variety of Na-, K-, Fe-, Ca-, Mn- and Ba-bearing chlorides/hydrochlorides, sulfides, arsenides magnetite, REE minerals and Fe-Ni alloys.

Peridotite whole rock Sr-Nd-Pb isotope data and U-Pb dating of metasomatic titanite support earlier suggestions that Ni mineralization is temporally and genetically related with the intrusion of the nearby 360 Ma Heemskirk Granite. It appears that the multiphase inclusions in metasomatic olivine demonstrate chemical signatures of both *in situ* serpentinites (entrapped alloys, sulfides, arsenides and magnetite) and distal fluids (enrichment in Pb, Bi, Sn, Sb, Sr, Ba, Rb, Cs and Ce).

We propose that magmatic olivine in large ultramafic bodies provides almost infinite Ni to replacive serpentinites and constitutes a major reservoir of disseminated Ni mineralization. In the case of Avebury Ni was locally redistributed from olivine in the Cambrian peridotites to mainly Fe-Ni alloys and sulfides during serpentinization in the early Paleozoic. In the Devonian reheating and interaction with a granitic fluid in the contact aureole of the Heemskirk Granite led to de-serpentinization and formation of metasomatic high-Mn, low-Ni olivine with inclusions of serpentine and entrapped alloys, sulfides, arsenides and magnetite, and metalliferous brines rich in ‘granitic’ elements. Nickel released from serpentinite in this process was re-deposited near the margins of the peridotite to form the Avebury Ni orebody. Our model of serpentinization-related

release of Ni from magmatic olivine, *in-situ* precipitation of metallic, sulfide and arsenide Ni-minerals, and their redistribution and recrystallization in hydrothermal conditions represents an alternative to Ni remobilization from magmatic sulfides.

Keywords: Ni sulfide deposits, peridotites, serpentinization, olivine, granite, metasomatism, geochronology.

INTRODUCTION

World nickel production depends on two main types of Ni deposits: magmatic and lateritic (Dill, 2010). Magmatic Ni deposits are mainly related to mafic and ultramafic rocks associated with layered intrusions, continental flood basalts and komatiites (e.g. Naldrett, 1999). Magmatic Ni sulfide deposits represent the magmatic accumulation of sulfide liquids immiscibly derived from mafic/ultramafic silicate melts (Naldrett, 1999). Laterite Ni deposits are formed on the Earth's surface due to extensive weathering of ultramafic rocks in tropical climates and related to the removal of Mg and Si and transportation and precipitation of a variety of Ni-bearing minerals (e.g. Butt and Cluzel, 2013; Elias, 2002).

In recent decades, a new class of Ni deposits - hydrothermal Ni sulfide - has received much attention, culminating in a special issue of Ore Geology Reviews (2013, v. 52; González-Álvarez et al., 2013). The Avebury deposit (Tasmania, Australia) is thought to represent a major example of this unconventional style of Ni mineralization (Keays and Jowitt, 2013). However, the petrogenesis of the Avebury mineralization remains controversial. According to Hoatson et al. (2006) this deposit bears "similarities to a hydrothermally modified magmatic sulfide deposit spatially associated with serpentinized ultramafic rocks". By contrast, Keays and Jowitt (2013)

69 favor an origin of the Ni (and Cu) by dissolution of disseminated magmatic sulfides at depth,
70 followed by metal re-precipitation from hydrothermal fluids at shallower levels.

71 Here we present the results of geochronological (U-Pb dating of hydrothermal titanite),
72 isotopic (Sr-Nd-Pb whole rock) and petrographic/mineral chemical studies (olivine, olivine-
73 hosted inclusions) of the Avebury Ni deposit. We present evidence for olivine which formed
74 from serpentine in the presence of metalliferous brines of complex origin. The role of several
75 populations of olivine in the Ni budget of the Avebury deposit is discussed. We suggest that
76 formation of serpentinite-related Ni ores was linked to mobilization of Ni from silicates rather
77 than from magmatic sulfides inferred to exist at depth.

78 ## AVEBURY NI SULFIDE DEPOSIT

79 The Avebury Ni sulfide deposit was discovered in 1997 near Zeehan, Tasmania, and it
80 was Australia's first economic nickel sulfide discovery outside of Western Australia (Hoatson et
81 al., 2006). As of January 2013, the Avebury resource was 18 Mt @ 1% Ni. Nickel-sulfide
82 mineralization (Fig. 1) is found in association with metasomatized ultramafic rocks (serpentinites
83 and diopside-tremolite metasomatites), and considered to be "hydrothermal-remobilized" in
84 origin (Hoatson et al., 2006; Keays and Jowitt, 2013; Keays et al., 2009; Lygin et al., 2010a).
85 Details of the geology, mineralogy and geochemistry of the ore bodies can be found in Callaghan
86 and Green (2014), Keays and Jowitt (2013) and Keays et al. (2009).

87 The host serpentinized peridotites (dunites and harzburgites) belong to the 516±0.9 Ma
88 (Mortensen et al., 2015) McIvor Hill mafic – ultramafic complex (Fig. 1). This and fifteen
89 neighboring ultramafic bodies, including the well-studied Heazlewood River complex (Peck,
90 1990), were emplaced into, or obducted onto, Neoproterozoic sedimentary sequences of a
91 passive continental margin in the Middle Cambrian (Berry and Crawford, 1988; Crawford and

Berry, 1992; Peck, 1990). The McIvor Hill complex was emplaced within a thick (> 5 km) late-Neoproterozoic sequence dominated by well-bedded greywacke with lesser black shale, siltstone, sandstone, limestone and volcaniclastic conglomerate containing clasts of basalts, andesites and rhyolites (Fig. 1). During the Late Devonian, the entire package of rocks was intruded by the large, multi-phase Heemskirk biotite-monzogranite (359.9±1.9 Ma, Black et al., 2005). Nickel mineralization at Avebury is located ~1.5 km southeast of the nearest granite exposure and only ~500 m above the shallowly-dipping top of the granite pluton, i.e. well within the contact aureole of the granite (Fig. 1). The mineralized zones are located along the margins of folded and faulted ultramafic rocks, in contact with metamorphosed and altered sediments (Fig. 1). Mineralogically-complex, skarn-like tremolite/actinolite-diopside lithologies, with locally significant boron mineralization (tourmaline, axinite, datolite), titanite and scheelite (Callaghan and Green, 2014; Keays and Jowitt, 2013) are attributed to reaction with granite-derived fluids (Keays and Jowitt, 2013; Keays et al., 2009; Lygin et al., 2010a). Strong enrichment (up to 5-6 orders of magnitude compared to lithophile elements of similar incompatibility) in "granitophile" elements (e.g., W, U, Pb, Bi, Mo, Sn and Sb) within the serpentinites is also attributed to the granite-derived fluids (Keays and Jowitt, 2013; Lygin et al., 2010b).

Avebury serpentinites are composed of antigorite, olivine, clino- and orthopyroxene, Cr-spinel, magnetite, pentlandite and pyrrhotite, with accessory awaruite Ni_3Fe, heazlewoodite (Ni_3S_2), millerite (NiS), gersdorffite NiAsS, maucherite ($Ni_{11}As_8$), and nickeline NiAs. Other minerals, atypical for serpentinites in general, are also present and include native gold and bismuth, arsenopyrite, pyrite, sphalerite, galena, bismuthinite, scheelite, wolframite, titanite, apatite, axinite and tourmaline. Importantly, the Ni arsenide mineralization extends beyond the Avebury deposit into the host sedimentary rocks for at least 300 m.

The Ni sulfide ore bodies are up to tens of meters thick and extend for hundreds of meters along inferred fault zones and faulted contacts of serpentinites and their host metasedimentary units. Pentlandite, often intergrown with magnetite, is the main sulfide mineral and is characterized by high Co (0.5 – 2.7 wt%) and a lack of platinum-group elements (PGE) (Lygin et al., 2010a). Pyrrhotite is also common, while Cu-rich sulfides are conspicuously rare. In comparison to typical orthomagmatic Ni-ores, the Avebury mineralization is poor in PGE (e.g. Pt < 6 ppb and Pd < 55 ppb) and Cu (< 550 ppm), but strongly enriched in Au, As, Bi, Pb, Sb and Sn (up to 0.4, 600, 350, 70, 120, 400 ppm, respectively; Keays and Jowitt, 2013).

SAMPLES AND METHODS

Although the peridotites hosting the Avebury deposit are pervasively serpentinized, fresh olivine with primary mineral and fluid inclusions was found in four samples in two drillholes (A193 and U066). Samples U066-12 and UO66-13 were collected on the boundary between serpentinite and diopside-tremolite metasomatite, ~20 meters from the contact between the ultramafic body and sedimentary country rocks. Samples A193-648.7 and A193-653.1 are from serpentinite well away (>100 m) from the contact with country rocks and ~40 meters away from the diopside-tremolite alteration zone.

Mineral textures and compositions, including those of olivine-hosted inclusions, were studied by electron microprobe, electron microscopy using secondary and back-scattered electron analysis and by laser ablation ICPMS, while whole-rock powders for samples U066-12 and U066-13 (and for three other peridotites) were used for Sm-Nd, Rb-Sr and U-Th-Pb isotope studies. Titanite in skarn-like assemblages in samples A193-502 and A193-519 was used for U-Th-Pb dating by laser ablation ICPMS. For this purpose, titanite (70-200 μm) was handpicked from heavy mineral concentrates and mounted in epoxy (see Fig.9).

Electron microprobe and electron microscope

Olivine compositions were obtained using a Cameca SX100 electron microprobe at the Central Science Laboratory, University of Tasmania. Analyses were done with 15 kV accelerating voltage and 30 nA beam current. Elements were acquired using Kα lines and analyzing crystals LLiF for Fe, Ni, LPET for Ca, PET for Cr, Mn, and TAP for Si, Mg. The standards were rhodonite for Mn, nickel silicide for Ni (both Astimex Scientific Ltd), San Carlos olivine for Si, Fe, Mg, Kakanui augite for Ca, and Tiebaghi chromite for Cr (Jarosewich et al., 1980). Peak and background counting times were 10 seconds for Fe, 20 seconds for Mg, Si, Cr, Mn, 30 seconds for Ni, and 40 seconds for Ca. The background correction method was slope (high) for Mn, and linear for all other elements. Oxygen was calculated by cation stoichiometry and included in the matrix correction (PAP algorithm). Detection limits (in wt%) were 0.01 for Ca, 0.02 for Mg, Si, 0.03 for Cr, Ni, 0.04 for Mn, and 0.05 for Fe. Analytical precision (in wt%) was 0.01 for Ca, 0.03 for Cr, Ni, 0.05 for Mn, and 0.2 for Mg, Si, and Fe.

Secondary electron (SE) and backscattered electron (BSE) images and energy dispersive X-ray spectrometry (EDS), including element maps, were acquired at 10kV accelerating voltage and 2 nA beam current on a Hitachi SU-70 Schottky field emission scanning electron microscope fitted with a Hitachi 5-segment solid state BSE detector and an Oxford IncaEnergy X-Max 80 silicon drift detector EDS system (CSL, University of Tasmania).

Laser ablation ICPMS

Semi- quantitative analyses of olivine-hosted inclusions were done using a Resonetics M50 HR 193 nm ArF excimer laser ablation system coupled to an Agilent 7500cs ICP-MS (CODES, University of Tasmania).. Selected inclusions (15-40 μm in diameter) found at depths of 10-60 μm in olivine were analyzed with laser spot sizes ranging from 19 to 46 μm depending

on the size of inclusions, a repetition rate of 10 Hz and an energy density of 3.5J/cm^2. Count rates were measured for the following isotopes: ^{11}B, ^{23}Na, ^{24}Mg, ^{27}Al, ^{29}Si, ^{31}P, ^{34}S, ^{35}Cl, ^{39}K, ^{43}Ca, ^{47}Ti, ^{53}Cr, ^{55}Mn, ^{57}Fe, ^{59}Co, ^{60}Ni, ^{65}Cu, ^{66}Zn, ^{75}As, ^{78}Se, ^{85}Rb, ^{88}Sr, ^{95}Mo, ^{118}Sn, ^{123}Sb, ^{133}Cs, ^{137}Ba, ^{140}Ce, ^{175}Lu, ^{182}W, ^{208}Pb, ^{209}Bi. Count rates were quantified using primary standard reference material (SRM) NIST 612 for all elements except Cl.

U-Th-Pb isotope analyses for titanite were obtained using the same instrumentation, with a 47 μm spot size, a repetition rate of 5 Hz and an energy density of 2.0 J/cm^2. Further details can be found in Appendix 1.

Whole rock Sm-Nd, Rb-Sr and U-Th-Pb isotope analyses

Radiogenic isotope analyses of Avebury peridotites were carried out by multi-collector ICPMS at the University of Melbourne, using methods adapted from Maas et al. (2005). Details can be found in Appendix 1.

RESULTS

The data essential for understanding the origin of the Avebury deposit, namely compositions of olivine and olivine-hosted multiphase inclusions, radiogenic isotope compositions of peridotites and geochronologic constraints, are presented below.

Avebury olivine and associated minerals

The peridotite samples selected here (Table 1) contain abundant olivine associated with mm-sized intergrowths of tremolite-diopside, Cr-spinel, magnetite and pentlandite (Fig. 2). Magnetite, variably enriched in Cr_2O_3, MnO, MgO and NiO (up to 15, 4, 2 and 1 wt%, respectively), forms several distinct but possibly related textural types: 1) euhedral inclusions in olivine, 2) overgrowths on and replacements along brittle fractures in Cr-spinel, 3) euhedral, often sintered grains cemented by pentlandite, and 4) lamellae-or "sheet"-like magnetite in

184 pentlandite which is possibly an exsolution or replacive feature (Fig. 2 D-E). "Dusty" magnetite
185 associates with serpentinized cracks in olivine (Fig. 2 B, C). Areas of coarse-grained anhedral
186 olivine are interspersed with patches and linear zones of intergrown magnetite and pentlandite
187 (Fig. 2 E, F). Most of the olivine in the studied samples appears to be heavily fragmented,
188 forming an interlocking mosaic of small, irregularly shaped grains that have the same
189 crystallographic orientation (Fig. 2 A-C). The spaces between the olivine fragments are filled
190 with serpentine and fine-grained magnetite (Fig. 2 A-C).

191 Most olivine fragments are highly variable in composition (Fe/Mg) on a local scale, as
192 readily seen in back-scattered electron (BSE) images (Fig. 2 A, C) where single fragments may
193 show strong and sharp contrasts in BSE intensity (Fig. 2C); at other times composition changes
194 gradually. Compositional domains may extend across the serpentinized fractures to other olivine
195 fragments (Fig. 2A). Areas of high fragmentation intensity, i.e. with the smallest olivine
196 fragments, tend to have the highest BSE intensity (higher Fe/Mg or lower Fo, Fig. 2A). Fe-rich
197 compositions are also common on the edges of several olivine fragments adjacent to the same
198 fracture.

199 The overall range in Fo content recorded in the internal areas of olivine fragments (edges
200 excluded) is 89-93 mol% (Fig. 3, Appendix 2). The majority of grains have 90.2-91.2 mol% Fo,
201 but strongly variable NiO (0.1-0.3 wt%) and MnO (0.4-1.4 wt%) abundances (Fig. 3, Appendix
202 2). Importantly, minor element and forsterite contents do not correlate, and MnO and NiO are
203 significantly higher and lower, respectively, than in olivine from subduction-related mafic
204 volcanics (boninites and low-Ti tholeiites), cumulates and mantle peridotites (Fig. 3). Although
205 the forsterite content of the Avebury olivine overlaps with that of olivine from the Heazlewood

River complex (78.4-93.7 mol %; Peck, 1990), it is lower in NiO and significantly more enriched in MnO (Fig. 3).

Olivine-hosted inclusions

Avebury olivine carries abundant primary (i.e. entrapped during olivine crystallization) inclusions that are neither typical fluid nor silicate melt inclusions (Fig. 4-6). Some grains contain many hundreds of tiny inclusions (<2 μm), making their host olivine turbid, whereas the larger inclusions (5 to 50 μm) are less abundant. Large inclusions are always associated with small inclusions and show no alignment with fractures or particular crystallographic orientations of host olivine (Fig. 4). They commonly have negative crystallographic shapes (Fig. 4-6) and contain several colorless, brownish and opaque crystalline and possibly vapor phases, however, a separate aqueous liquid phase was not observed. Optical recognition of crystalline phases in transmitted light was not successful due to their small sizes, complex intergrowths and isotropic properties.

Inclusions were studied on polished surfaces of olivine (Fig. 4B, 5, 6, Appendix 3). Several hundred olivine grains (0.2-0.4 mm) hand-picked from crushed peridotites were mounted in epoxy resin and hand-polished using kerosene as a lubricant, to prevent damage to water-soluble phases. Final polishing was done on a silk-covered surface using an oil-based, water-free 1 μm diamond compound. After exposure the samples were carbon-coated and stored in a desiccator to avoid interaction with atmospheric moisture.

Inclusions located within < 1 μm of the polished olivine surfaces decrepitate and exude a brine-like substance of dominantly Ca-chloride composition with minor Na, K, Fe and Mg (Fig. 5A). A characteristic feature of exposed inclusions is a large number of solid phases (from 2 to 10-15) of varying sizes and highly variable proportions of these phases (at least at exposed

229 surfaces; Fig. 5). A fibrous Mg-silicate mineral, most likely serpentine, soaked in a multi-
230 element chloride liquid, is present in most studied inclusions and occupies up to 90% of the host
231 inclusion's volume (Fig. 5 B-E). Other abundant phases (up to 80 vol%) are represented by
232 chloride and hydrochloride minerals, ranging from common halite and sylvite to Fe-rich
233 compositions, dominated by Fe-Mn and Fe-Mg-Mn. Chlorides of Ba (±Sr) and Mg-K (±Cs) are
234 also common, but smaller in size, whereas minute (<1-2 μm) chlorides, sulfides, arsenides and
235 alloys, containing Fe, Ni, Cu, Zn and Pb, occur sporadically (Fig. 5). In most cases the small size
236 of Ni-bearing phases (Ni-As, Ni-As-S, Ni-Fe-S, Ni-Fe-Cl, Ni_3Fe, Ni_2Pb) suggests *in situ* growth
237 (i.e. daughter phases, Fig. 5 D, G, H), however, disproportionally large Ni-bearing grains (e.g.
238 Ni-Fe-S, Fig. 5F), magnetite, Cr-bearing magnetite (Appendix 3) and REE-rich phases
239 (monazite, bastnäesite, florencite) in the olivine suggest that these phases were present as solids
240 in the parental media (discussed below) at the time of olivine growth.
241 The mineral assemblage observed in exposed inclusions was further examined by LA-
242 ICP-MS analysis of thirty unexposed, multiphase inclusions > 15 μm in size. In the absence of
243 internal standardization (i.e. no other analytical methods can be applied prior to LA-ICP-MS),
244 inter-element ratios are readily obtained (Fig.7) but absolute element abundances cannot be
245 calculated with high precision. Given that the non-silicate component of the inclusions is
246 dominantly chloridic, apparent elemental compositions were normalized to 50 wt% total
247 chlorides to improve quantitation (Appendix 4). With this approach, the brine component is
248 dominated by Na (5-8 wt%), K (2-6 wt%), Ca (3-7 wt%), Fe (2-13 wt%) and Mn (0.4-1.4 wt%).
249 Higher relative abundances of Fe+Mn come at the expense of lower Na+K and Ca (Fig. 7).
250 The analyzed inclusions also contain (with upper limits given) boron (<600 ppm),
251 alkaline earth (Sr <1300 ppm and Ba <7500 ppm), and alkaline metals (Rb <650 ppm, Cs < 500

ppm, Rb and Cs well correlated, Fig. 7). The abundances of some chalcophile metals (Pb < 4000 ppm, Zn < 2400 ppm, and Ni <3300 ppm, Fig. 7) are highly elevated compared to common silicate rocks and hydrothermal fluids, but other metals such as Co and Cu (both < 200 ppm) are not anomalous. Concentrations of S (< 2700 ppm) are roughly proportional to those of the chalcophile metals. In general, Co, Ni and Cr are highly variable and reflect small-volume Ni- and Cr-bearing phases. Other elements (e.g., As, Sn, Sb, Ce, W and Bi) are commonly present at 10s-100s of ppm (Appendix 4).

Radiogenic isotopes

The analyzed peridotites have low REE contents and high, near-chondritic Sm/Nd (Table 1). Present-day $^{143}Nd/^{144}Nd$ shows little range (0.51245-0.51249), equivalent to present-day ε_{Nd} values of -3.5 to -2.7. By contrast, Rb/Sr varies strongly (0.25-3.73) and measured $^{87}Sr/^{86}Sr$ is high (0.7231-0.7738). In the Rb-Sr isochron diagram (not shown) the data points form a scattered (MSWD 181) but extensive array with a slope equivalent to an age of 357±14 Ma ($^{87}Sr/^{86}Sr_i$ ~0.7195).

The U-Th-Pb systematics of the rocks (Table 1) are characterized by remarkably high Pb contents (4.4-32 ppm), very low Th/U (0.27-0.39) and low $^{238}U/^{204}Pb$ (0.61-6.07) and $^{232}Th/^{204}Pb$ (0.17-2.25) ratios, suggesting addition of Pb and U to the rocks. Measured Pb isotope ratios show narrow ranges (18.490-18.708, 15.638-15.648, 38.390-38.436; Table 1, Fig. 8) and there is little correlation in U-Pb, Th-Pb and Pb-Pb isotope plots.

Titanite geochronology

Laser ablation ICPMS spot analyses for titanite from two skarn-like assemblages show highly variable U/Pb and Pb isotope ratios, covering the entire range from almost pure radiogenic to entirely common Pb (Fig. 9). The data for both analyzed grain populations plot on

the same scattered trend (Fig. 9), with individual lower intercept ages of 369±16 and 366±6 Ma, respectively. Ablation profiles (30 second ablation time) for the titanite are characterized by extreme heterogeneity, oscillating rapidly between radiogenic- and common Pb-dominated segments. Trace-element data collected along traverses across the same crystals using a smaller spot size (26 μm) show them to contain domains with high contents of Pb, Zn, Ba, K and Cs which are interpreted to represent small (<5 μm) galena and fluid inclusions trapped within the crystals. While overall averages of the U-Th-Pb isotope analyses for each analytical spot are shown in Fig.9A, Fig. 9B shows the same data after splitting the U-Pb ablation profiles into 8 segments, increasing both the number of data points and, more importantly, the dispersion along the radiogenic-common Pb mixing line, potentially improving age precision (e.g. Davidson et al., 2007; Petrus and Kamber, 2012). The pooled results for all available ablations yield an age of 363±3 Ma, with an upper intercept $^{207}Pb/^{206}Pb$ of 0.8438.

ORIGIN OF THE AVEBURY NI SULFIDE DEPOSIT

Was the granite involved?

The Late Devonian Heemskirk Granite is well-known for having evolved a major late-magmatic fluid phase and is associated with numerous hydrothermal mineral (Sn, Pb, Ag, Zn) deposits located within its (hydrothermal) contact aureole (e.g. McClenaghan, 2006 and references therein). Granite-related tourmalinization is widespread both within and around the granite. Hydrothermal Ni sulfide mineralization at Avebury has therefore been linked with granite-related overprinting of the McIvor Hill Complex ultramafic rocks in all previous studies which have documented the unusual enrichment in lithophile and other granitophile elements at Avebury (e.g. Keays and Jowitt, 2013; Lygin et al., 2010b).

297 The results presented here provide further evidence for the granite link. Hydrothermal
298 titanite and whole-rock Rb-Sr isotopic data document a ~360 Ma event interpreted here as the
299 age of major alteration within the peridotites. The age of this alteration is indistinguishable from
300 U-Pb zircon emplacement ages for the Heemskirk Granite (361±2 and 360±2 Ma; Black et al.,
301 2005). Sr-Nd isotope data also support overprinting by granitic fluids: $^{87}Sr/^{86}Sr$ and ε_{Nd} in the
302 peridotites, calculated at 360 Ma (0.7189-0.7202, -2.8 to -4.0, Table 1) are similar to the Sr-Nd
303 isotope signatures in the two phases of the Heemskirk Granite (I-type Heemskirk Red, 0.7114/-
304 4.8; S-type Heemskirk White, 0.7397, -7.7; Black et al., 2010).
305 Initial Pb isotope ratios for the two phases of the Heemskirk Granite are 17.59, 15.56,
306 38.50 (Heemskirk White) and 18.68, 15.61, 38.54 (Heemskirk Red, Black et al., 2010). These
307 data may not be reliable because they are based on whole rocks with high U/Pb ($^{238}U/^{204}Pb$ 52.6,
308 36.1) and Th/Pb ($^{232}Th/^{204}Pb$ 64.5, 164) ratios, rather than on low-U/Pb materials such as
309 feldspars. By contrast, $^{238}U/^{204}Pb$ - $^{232}Th/^{204}Pb$ ratios in the analyzed Avebury peridotites are
310 ≤6.1 and ≤2.25, respectively. The granite Pb isotope data are therefore unsuitable for detailed
311 comparison with the Avebury data. However, the latter (both the high precision whole rock data
312 and the initial $^{207}Pb/^{206}Pb$ inferred from analysis of Pb-rich impurities in titanite by laser ablation
313 ICPMS) are similar to initial Pb isotope compositions for Late Devonian (granite-related)
314 sulfides of the nearby Zeehan Ag-Pb-Zn mineral field which is clearly related to the Heemskirk
315 Granite (Fig. 8). The Avebury data plot near the unradiogenic end of the Zeehan Pb isotope
316 range, suggesting possible mixing of Devonian and older (Cambrian ?) ore lead within the
317 granite-related fluids that interacted with the peridotites . One of the five peridotite whole rock
318 analyses (#A12) produced a lower $^{206}Pb/^{204}Pb_{360\ Ma}$ which plots closer to the field for Cambrian
319 (volcanogenic massive sulfide) mineralization (Gulson et al., 1987; Gulson and Porritt, 1987;

Münker, 2000; Solomon et al., 2004). By contrast, calculated initial $^{207}Pb/^{204}Pb$ and $^{208}Pb/^{204}Pb$ (both are rather insensitive to the age corrections) for this sample are not anomalous; it is therefore possible that the low $^{206}Pb/^{204}Pb$ is an artifact of the age correction.

Metasomatic origin of Avebury peridotites

We argue for a metasomatic origin of the Avebury olivine based on unusual compositional features, mineral association and presence of primary multiphase inclusions. Comparison with the Heazlewood River ultramafic complex (Peck, 1990), considered to be an unaltered analogue of the Avebury ultramafic rocks (Keays and Jowitt, 2013), shows that most of the Avebury olivine grains are significantly more enriched in MnO (0.4-1.4 wt%) and depleted in NiO (0.1-0.3 wt%) for a given Fo content (c.f. 0.1 and 0.4 wt%, respectively, in the Heazlewood River olivine, Fig. 3). Likewise, similar contrasts exist when Avebury olivine is compared to compositions of olivine phenocrysts in a number of boninites and arc low-Ti basalts (Fig. 3) that may represent parental melts for the olivine-rich cumulates of the Heazlewood River complex (Crawford and Berry, 1992; Peck, 1990). Avebury olivine does not show the typical correlations of Fo content with MnO (negative) and NiO (positive) that are typical of magmatic olivine (Fig. 3). On the other hand, unusually high MnO abundances in Avebury olivine mirror the high MnO in olivine formed by de-serpentinization (e.g. Frost, 1975; O'Hanley, 1996; Pinsent and Hirst, 1977; Vance and Dungan, 1977).

The primary inclusion suite found in the Avebury olivine (Fig. 4-6, Appendix 3) has no known analogue in olivine from the Heazlewood River or indeed in any other mafic and ultramafic suite in Tasmania or globally. These inclusions are distinct from all olivine-hosted inclusions studied to date in having an assemblage of fibrous Mg-silicate (serpentine-like) minerals and chloride-rich solid and aqueous phases (Fig. 5 B-H). The variable proportions of

these phases in neighboring inclusions are complemented by significant differences in the composition of the chloride component (Fig. 7).

Moreover, the presence of magnetite, Fe-Ni-Cu sulfides and REE-rich minerals inside the inclusions (Fig. 5) and the presence of magnetite and apatite as inclusions in olivine (Fig. 2B) suggest that the Avebury olivine formed in a medium that is highly heterogeneous on a grain-scale. Based on the inclusions' phase compositions, the latter was dominated by serpentine-like minerals "soaked" in a multi-element chloride solution (brine). We propose that the Avebury olivine formed at the expense of serpentine in the presence of a saline aqueous fluid (brine). This mode of olivine formation, involving a precursor hydrated Mg-silicate crystalline phase and hydrous solutions, is neither magmatic (i.e. formed from a melt) nor metamorphic (solid state re-crystallization) nor hydrothermal (deposition from aqueous fluid), and thus the Avebury olivine is best described as "metasomatic".

From magmatic cumulates to mineralized metasomatites: a storyline

The association of ~~the~~ Avebury Ni sulfide mineralization with metasomatic olivine and contact metasomatic assemblages suggests that the present Ni ores were formed though a combination of suitable precursor rocks and favorable magmatic, metamorphic, metasomatic and mineralizing processes. We propose several stages in the development of the Ni sulfide mineralization, each consecutive stage being reliant on the completion of the previous stage.

Partially to completely serpentinized dunites and harzburgites of the Heazlewood River complex contain 0.13-0.36 wt% NiO that is mainly stored in olivine, sulfides and alloys. Whereas the Heazlewood River olivine is primary, other nickeliferous minerals and associated magnetite are fine-grained phases (<20 μm), dispersed throughout mesh-textured, fibrous serpentine along boundaries of pseudomorphed olivine (Peck, 1990). The Ni contents of the host

366 rocks do not correlate with the degree of serpentinization. This suggests that in this (Peck, 1990)
367 and other suites of serpentinized peridotites (e.g. Auclair et al., 1993; Chamberlain, 1966;
368 Eckstrand, 1975; Guillon and Lawrence, 1973; Nickel, 1959; O'Hanley, 1996; Ramdohr, 1967;
369 Sciortino et al., 2015) the main Ni-rich minerals – heazlewoodite (first described in 1896 from
370 Lord Brassey Mine, Heazlewood River complex (i.e. type locality), see
371 http://www.mindat.org/min-1839.html), pentlandite, millerite and awaruite – contain Ni derived
372 in situ from alteration of primary olivine. The initial serpentinization of the Heazlewood River
373 complex is proposed to occur during its tectonic emplacement into the uppermost crust and
374 interaction with seawaters in the Middle Cambrian (Rubenach, 1973), followed by major
375 serpentinization in the Ordovician and Early Devonian (Peck, 1990).

376 We note, based on the NiO abundances in the Heazlewood River peridotites, that
377 completely serpentinized dunites and harzburgites of the McIvor Hill complex may have
378 contained ~ 3.5-10 kg/m^{3}of Ni, stored mainly in sulfides and alloys and partly in magnetite and
379 serpentine. The inclusions of serpentine found in the Avebury olivine in association with
380 chlorides and hydrochlorides (Fig. 5) are considered to represent a relic environment, where
381 further accumulation of Ni sulfides has taken place. In other words, liberation of Ni from
382 primary silicate minerals combined with wholesale enrichment in chlorine during sea-floor
383 serpentinization (e.g. Early, 1958; Miura et al., 1981; Orberger et al., 1999; Rucklidge and
384 Patterson, 1977; Scambelluri et al., 1997) were prerequisite factors conducive to later sulfide
385 upgrading.

386 In the Late Devonian, the heat and fluids derived from the intrusion of the Heemskirk
387 Granite caused significant transformations in outer zones of the McIvor Hill ultramafic body, the
388 host of the Avebury deposit. There is broad agreement that high abundances of non-peridotite

389 elements (alkali and alkali-earth elements, W, U, Pb, Bi, Sn, Sb, As, S and Au) in the Avebury
390 peridotites and spatially associated mineralization are related to interaction with fluids derived
391 from the nearby granite and from local metasedimentary rocks (Keays and Jowitt, 2013; Keays et
392 al., 2009; Lygin et al., 2010a). Keays and Jowitt (2013) further suggested that the granitic-
393 hydrothermal fluids dissolved primary magmatic Ni sulfides inferred to have been present at
394 depth, and transferred their metal budget to the margins of the ultramafic body to form the
395 Avebury ore. However, our results on compositionally unusual olivine (Fig. 3) and olivine-
396 hosted inclusions (Fig. 4-6) provide a background for an alternative source of Ni. We suggest
397 that the pre-Late Devonian serpentinite experienced de-watering and recrystallization to olivine
398 in response to the granite emplacement. The de-serpentinization process, relatively common in
399 other peridotites (e.g. Neumann et al., 2015; O'Hanley, 1996 and references therein), has a
400 potential of purging non-silicate components, which in the case of Avebury were Cr-spinel,
401 magnetite and Ni- and Ni-Fe sulfides and alloys. It cannot be excluded that in addition to such
402 mechanical “cleansing”, Ni was transported and deposited by aqueous saline fluids (e.g. Tian et
403 al., 2013 and references therein), both serpentinite- and granite-derived. Re-precipitation of Ni
404 and accumulation of Ni-minerals were likely controlled by geochemical barriers, thus zones of
405 mineralized rocks mainly extend along the contacts of the ultramafic body with country rocks
406 (Keays and Jowitt, 2013). The role of fluid transport of Ni can be seen beyond the Avebury
407 deposit in a significant aureole of Ni arsenide mineralization extending at least 300 m into the
408 regional sediments.

409 ## IMPLICATIONS

410 Our genetic model of the Avebury Ni-sulfide deposit involves one source of Ni and three
411 main stages of Ni buildup:

1) Accumulation of Ni in magmatic olivine and sulfides in dunites and harzburgites of the Cambrian McIvor Hill complex;

2) Formation of disseminated Ni sulfides and alloys in response to serpentinization of ultramafic rocks in the pre-Late Devonian;

3) Transport of Ni both in solution and as previously formed minerals, both originally magmatic and formed during serpentinization, to suitable trap-sites in response to de-serpentinization, related to emplacement of the Heemskirk granite in the Late Devonian.

Our model has elements in common with that of Keays and Jowitt (2013). The major difference lies in the recognition of a previously unrecognized source of Ni within the McIvor Hill ultramafic complex. Magmatic olivine in voluminous ultramafic bodies provides almost infinite Ni to replacive serpentinites, dwarfing potential contribution from magmatic sulfides. The entire Ni content of the deposit (180 million kg) could potentially be supplied by mobilizing part of the Ni content of 1 km^3 of serpentinite. Given such relatively modest source volumes, the pervasive granite-related metasomatism, and the presence of Ni-depleted metasomatic olivine with remnant serpentinite inclusions at Avebury implies that olivine-derived Ni was indeed mobilized from local serpentinites and reconcentrated within the ore lenses in response to chemical and other gradients.

ACKNOWLEDGMENTS

Marcel Guillong and Sarah Gilbert are thanked for assistance with laser ablation ICP-MS analyses. MMG (Minerals and Metals Group) provided access to drill-core and geological materials and supported this publication. Constructive comments by an anonymous reviewer and Jim Webster and editorial handling by Julie Roberge are greatly appreciated. This study was

434 funded by the ARC Centre of Excellence in Ore Deposits to AVL and JGF and the ARC
435 Discovery Grant to VSK.

436 **REFERENCES CITED**

437 Auclair, M., Gauthier, M., Trottier, J., Jebrak, M., and Chartrand, F. (1993) Mineralogy,
438 geochemistry, and paragenesis of the Eastern Metals serpentinite-associated Ni-Cu-Zn
439 deposit, Quebec Appalachians. Economic Geology, 88, 123-138.
440 Berry, R.F., and Crawford, A.J. (1988) The tectonic significance of Cambrian allochthonous
441 mafic-ultramafic complexes in Tasmania. Australian Journal of Earth Sciences, 35, 523-
442 533.
443 Black, L.P., Everard, J.L., McClenaghan, M.P., Korsch, R.J., Calver, C.R., Fioretti, A.M.,
444 Brown, A.V., and Foudoulis, C. (2010) Controls on Devonian-Carboniferous magmatism
445 in Tasmania, based on inherited zircon age patterns, Sr, Nd and Pb isotopes, and major
446 and trace element geochemistry. Australian Journal of Earth Sciences, 57, 933-968.
447 Black, L.P., McClenaghan, M.P., Korsch, R.J., Everard, J.L., and Foudoulis, C. (2005)
448 Significance of Devonian-Carboniferous igneous activity in Tasmania as derived from U-
449 Pb SHRIMP dating of zircon. Australian Journal of Earth Sciences, 52, 807-829.
450 Butt, C.R.M., and Cluzel, D. (2013) Nickel laterite ore deposits: Weathered serpentinites.
451 Elements, 9, 123-128.
452 Callaghan, T., and Green, G.R. (2014) Avebury nickel deposits. In K.D. Corbett, P.G. Quilty,
453 and C.R. Calver, Eds. Geological Evolution of Tasmania, Special Publication 24, p. 357-
454 361. Geological Society of Australia.
455 Chamberlain, J.A. (1966) Heazlewoodite and awaruite in serpentinites of the Eastern Townships,
456 Quebec. Canadian Mineralogist, 8.

457 Crawford, A.J., and Berry, R.F. (1992) Tectonic implications of Late Proterozoic - Early
458 Palaeozoic igneous rock associations in western Tasmania. Tectonophysics, 214, 37-56.
459 Davidson, G.J., Paterson, H., Meffre, S., and Berry, R.F. (2007) Characteristics and origin of the
460 oak dam East Breccia-Hosted, iron oxide Cu-U-(Au) Deposit: Olympic Dam region,
461 Gawler Craton, South Australia. Economic Geology, 102, 1471-1498.
462 Dill, H.G. (2010) The "chessboard" classification scheme of mineral deposits: Mineralogy and
463 geology from aluminum to zirconium. Earth-Science Reviews, 100, 1-420.
464 Early, J.W. (1958) On chlorine in serpentinized dunite. American Mineralogist, 43, 148-155.
465 Eckstrand, O.R. (1975) The Dumont serpentinite: A model for control of nickeliferous opaque
466 mineral assemblages by alteration reactions in ultramafic rocks. Economic Geology, 70,
467 183-201.
468 Elias, M. (2002) Nickel laterite deposits – a geological overview, resources and exploitation.
469 Centre for Ore Deposit Research Special Publication 4, p. 205-220. University of
470 Tasmania, Hobart.
471 Frost, B.R. (1975) Contact metamorphism of serpentinite, chloritic blackwall and rodingite at
472 paddy-go-easy pass, central cascades, Washington. Journal of Petrology, 16, 272-313.
473 González-Álvarez, I., Pirajno, F., and Kerrich, R. (2013) Hydrothermal nickel deposits: Secular
474 variation and diversity. Ore Geology Reviews, 52, 1-3.
475 Guillon, J.H., and Lawrence, L.J. (1973) The opaque minerals of the ultramafic rocks of New
476 Caledonia. Mineralium Deposita, 8, 115-126.
477 Gulson, B.L., Large, R.R., and Porritt, P.M. (1987) Base metal exploration of the Mount Read
478 volcanics, western Tasmania: III. Application of lead isotopes at Elliott Bay. Economic
479 Geology, 82, 308-327.

480 Gulson, B.L., and Porritt, P.M. (1987) Base metal exploration of the Mount Read volcanics,
481 western Tasmania: II. Lead isotope signatures and genetic implications. Economic
482 Geology, 82, 291-307.
483 Hoatson, D.M., Jaireth, S., and Jaques, A.L. (2006) Nickel sulfide deposits in Australia:
484 Characteristics, resources, and potential. Ore Geology Reviews, 29, 177-241.
485 Jarosewich, E.J., Nelen, J.A., and Norberg, J.A. (1980) Reference samples for electron
486 microprobe analysis. Geostandards Newsletter, 4, 43-47.
487 Kamenetsky, V.S., Binns, R.A., Gemmell, J.B., Crawford, A.J., Mernagh, T.P., Maas, R., and
488 Steele, D. (2001a) Parental basaltic melts and fluids in eastern Manus backarc basin:
489 Implications for hydrothermal mineralisation. Earth and Planetary Science Letters, 184,
490 685-702.
491 Kamenetsky, V.S., Crawford, A.J., Eggins, S.M., and Mühe, R. (1997) Phenocrysts and melt
492 inclusion chemistry of near-axis seamounts, Valu Fa Ridge, Lau Basin: insight into
493 mantle wedge melting and the addition of subduction components. Earth and Planetary
494 Science Letters, 151, 205-223.
495 Kamenetsky, V.S., Crawford, A.J., and Meffre, S. (2001b) Factors controlling chemistry of
496 magmatic spinel: an empirical study of associated olivine, Cr-spinel and melt inclusions
497 from primitive rocks. Journal of Petrology, 42, 655-671.
498 Kamenetsky, V.S., Sobolev, A.V., Eggins, S.M., Crawford, A.J., and Arculus, R.J. (2002)
499 Olivine-enriched melt inclusions in chromites from a low-Ca boninite, Cape Vogel,
500 Papua New Guinea: evidence for ultramafic primary magma, refractory mantle source
501 and enriched components. Chemical Geology, 183, 287-303.

Keays, R.R., and Jowitt, S.M. (2013) The Avebury Ni deposit, Tasmania: A case study of an unconventional nickel deposit. Ore Geology Reviews, 52, 4-17.

Keays, R.R., Jowitt, S.M., and Callaghan, T. (2009) The Avebury Ni deposit, Tasmania: a case study of an unconventional nickel deposit. In P.J. Williams, Ed. Smart Science for Exploration and Mining, Proceedings of the Tenth Biennial SGA Meeting, p. 173-175, Townsville, Australia.

Lygin, A.V., Foster, J.G., and Hutchinson, D. (2010a) A new style of Ni-mineralization resulting from the interaction of ultramafic rocks with hydrothermal fluids derived from granites: Avebury Ni-deposit, Western Tasmania. 11th International Platinum Symposium, Miscellaneous Release-Data, vol. 269. Ontario Geological Survey, Sudbury, Ontario.

Lygin, A.V., Foster, J.G., Hutchinson, D., and Callaghan, T. (2010b) The mineralogy and geochemistry of the Avebury Ni-deposit, Western Tasmania. 13th Quadrennial IAGOD Symposium, p. 96-97, Adelaide, Australia.

Maas, R., Kamenetsky, M.B., Sobolev, A.V., Kamenetsky, V.S., and Sobolev, N.V. (2005) Sr, Nd, and Pb isotope evidence for a mantle origin of alkali chlorides and carbonates in the Udachnaya kimberlite, Siberia. Geology, 33, 549–552.

McClenaghan, M.P. (2006) The geochemistry of Tasmanian Devonian–Carboniferous granites and implications for the composition of their source rocks, Record 2006/06, p. 31. Tasmanian Geological Survey.

Miura, Y., Rucklidge, J., and Nord, G.L. (1981) The occurrence of chlorine in serpentine minerals. Contributions to Mineralogy and Petrology, 76, 17-23.

523 Mortensen, J.K., Gemmell, J.B., McNeill, A.W., and Friedman, R.M. (2015) High-precision U-
524 Pb zircon chronostratigraphy of the Mount Read Volcanic belt in Western Tasmania,
525 Australia: Implications for VHMS deposit formation. Economic Geology, 110, 445-468.
526 Münker, C. (2000) Pb-Nd isotopes indicate the origin of Island Arc Terranes in the early
527 Paleozoic Pacific. Journal of Geology, 108, 233-242.
528 Naldrett, A.J. (1999) World-class Ni-Cu-PGE deposits: key factors in their genesis. Mineralium
529 Deposita, 34, 227-240.
530 Neumann, E.R., Abu El-Rus, M.A., Tiepolo, M., Ottolini, L., Vannucci, R., and Whitehouse, M.
531 (2015) Serpentinization and deserpentinization reactions in the upper mantle beneath
532 Fuerteventura revealed by peridotite xenoliths with fibrous orthopyroxene and mottled
533 olivine. Journal of Petrology, 56, 3-31.
534 Nickel, E.H. (1959) The occurrence of native nickel-iron in the serpentine rock of the Eastern
535 Townships of Quebec Province. Canadian Mineralogist, 6, 307-319.
536 O'Hanley, D.S. (1996) Serpentinites: Records of tectonic and petrological history. Oxford
537 University Press.
538 Orberger, B., Metrich, N., Mosbah, M., Mevel, C., and Fouquet, Y. (1999) Nuclear microprobe
539 analysis of serpentine from the Mid-Atlantic Ridge. Nuclear Instruments & Methods in
540 Physics Research Section B-Beam Interactions with Materials and Atoms, 158, 575-581.
541 Peck, D.C. (1990) The platinum-group element geochemistry and petrogenesis of the
542 Heazlewood River mafic-ultramafic complex, Tasmania, PhD thesis, p. 566. University
543 of Melbourne.

544 Petrus, J.A., and Kamber, B.S. (2012) VizualAge: A Novel Approach to Laser Ablation ICP-MS
545 U-Pb Geochronology Data Reduction. Geostandards and Geoanalytical Research, 36,
546 247-270.
547 Pinsent, R.H., and Hirst, D.M. (1977) The metamorphism of the Blue River ultramafic body,
548 Cassiar, British Columbia, Canada. Journal of Petrology, 18, 567-594.
549 Ramdohr, p. (1967) A widespread mineral association, connected with serpentinization. Neues
550 Jahrbuch Mineralogie Abhandlungen, 107, 241-265.
551 Rubenach, M.J. (1973) The Tasmanian ultramafic-gabbro and ophiolite complexes, PhD thesis,
552 p. 213. University of Tasmania.
553 Rucklidge, J.C., and Patterson, G.C. (1977) The role of chlorine in serpentinization.
554 Contributions to Mineralogy and Petrology, 65, 39-44.
555 Scambelluri, M., Piccardo, G.B., Philippot, P., Robbiano, A., and Negretti, L. (1997) High
556 salinity fluid inclusions formed from recycled seawater in deeply subducted alpine
557 serpentinite. Earth and Planetary Science Letters, 148, 485-499.
558 Sciortino, M., Mungall, J.E., and Muinonen, J. (2015) Generation of High-Ni sulfide and alloy
559 phases during serpentinization of dunite in the Dumont sill, Quebec. Economic Geology,
560 110, 733-761.
561 Sigurdsson, I.A., Kamenetsky, V.S., Crawford, A.J., Eggins, S.M., and Zlobin, S.K. (1993)
562 Primitive island arc and oceanic lavas from the Hunter ridge-Hunter fracture zone.
563 Evidence from glass, olivine and spinel compositions. Mineralogy and Petrology, 47,
564 149-169.
565 Solomon, M., Gemmell, J.B., and Zaw, K. (2004) Nature and origin of the fluids responsible for
566 forming the Hellyer Zn-Pb-Cu, volcanic-hosted massive sulphide deposit, Tasmania,

using fluid inclusions, and stable and radiogenic isotopes. Ore Geology Reviews, 25, 89-124.

Stacey, J.S., and Kramers, J.D. (1975) Approximation of terrestrial lead isotope evolution by a two-stage model. Earth and Planetary Science Letters, 26, 207-221.

Tian, Y., Etschmann, B., Liu, W., Borg, S., Mei, Y., Testemale, D., O'Neill, B., Rae, N., Sherman, D.M., Ngothai, Y., Johannessen, B., Glover, C., and Brugger, J. (2013) Speciation of nickel (II) chloride complexes in hydrothermal fluids: In situ XAS study. Chemical Geology, 334, 345-363.

Vance, J.A., and Dungan, M.A. (1977) Formation of peridotites by deserpentinization in Darrington and Sultan areas, Cascade Mountains, Washington. Geological Society of America Bulletin, 88, 1497-1508.

FIGURE CAPTIONS

Fig. 1. Schematic cross-section through magmatic and sedimentary rock units containing the Avebury deposit. For a regional map and more details of regional geology and tectonic history see paper by Keays and Jowitt (2013).

Fig. 2. Backscattered electron images showing main petrographic and mineralogical features of the Avebury peridotites. A-C: Metasomatic olivine with strong compositional heterogeneity (darker and brighter areas are higher and lower in Fo content, respectively) is cut by fractures with serpentine and fine-grained magnetite. Note apatite (Ap) inclusions in olivine (B). D-F: Metasomatic-hydrothermal assemblages of magnetite (Mt) replacing Cr-spinel (Cr) and magnetite - pentalandite (Pn) – tremolite (Tr) intergrowths. Scale bars are 100 μm.

589 Fig. 3. Compositions of Avebury metasomatic olivine (circles) compared to compositions of
590 olivine from the Heazelwood River complex peridotites (two samples, crosses) and olivine from
591 boninites and island-arc tholeiites (field; Kamenetsky et al., 2001a; Kamenetsky et al., 1997;
592 Kamenetsky et al., 2001b; Kamenetsky et al., 2002; Sigurdsson et al., 1993). Compositional data
593 can be found in Appendix 1.
594 Fig. 4. Transmitted light (A) and backscattered electron (B) images of Avebury metasomatic
595 olivine containing multiphase inclusions.
596 Fig. 5. Backscattered electron images of Avebury metasomatic olivine showing Ca-rich brine on
597 the surface (A) and exposed multiphase inclusions (B-H). The phases in inclusions are serpentine
598 (S), halite (NaCl), sylvite (KCl), complex chlorides and hydrochlorides containing Ba (±Sr, Cs),
599 Fe, Fe-Mn, Fe-Mn-Mg, Ca-Fe and K-Mn ((±Mg), magnetite (Mt), Fe-Ni sulfides and sulfides
600 and arsenides of Ni, Zn, Pb (±Cu). EDS X-ray element maps of some exposed inclusions are
601 presented in Fig. 6 and Appendix 2.
602 Fig. 6. Backscattered electron image and X-ray element maps of the olivine-hosted inclusion (see
603 Fig. 5D for phase identification).
604 Fig. 7. Ternary diagrams showing bulk element compositions (in wt%) of the olivine-hosted
605 inclusions.
606 Fig. 8. Initial isotope compositions of the Avebury peridotite compared to various ores and
607 galena from western Tasmania. Data for the Zeehan mineral field from (Gulson and Porritt,
608 1987) and unpublished reports.
609 Fig. 9. Tera-Wasserburg diagram for Avebury titanite (shown on the BSE image) from two
610 samples; A: average compositions s from individual analyses. B: each LA-ICPMS analyses are
611 divided into 8 separate segments (see text for details).

This is a preprint, the final version is subject to change, of the American Mineralogist (MSA)
Cite as Authors (Year) Title. American Mineralogist, in press.
(DOI will not work until issue is live.) DOI: http://dx.doi.org/10.2138/am-2016-5509

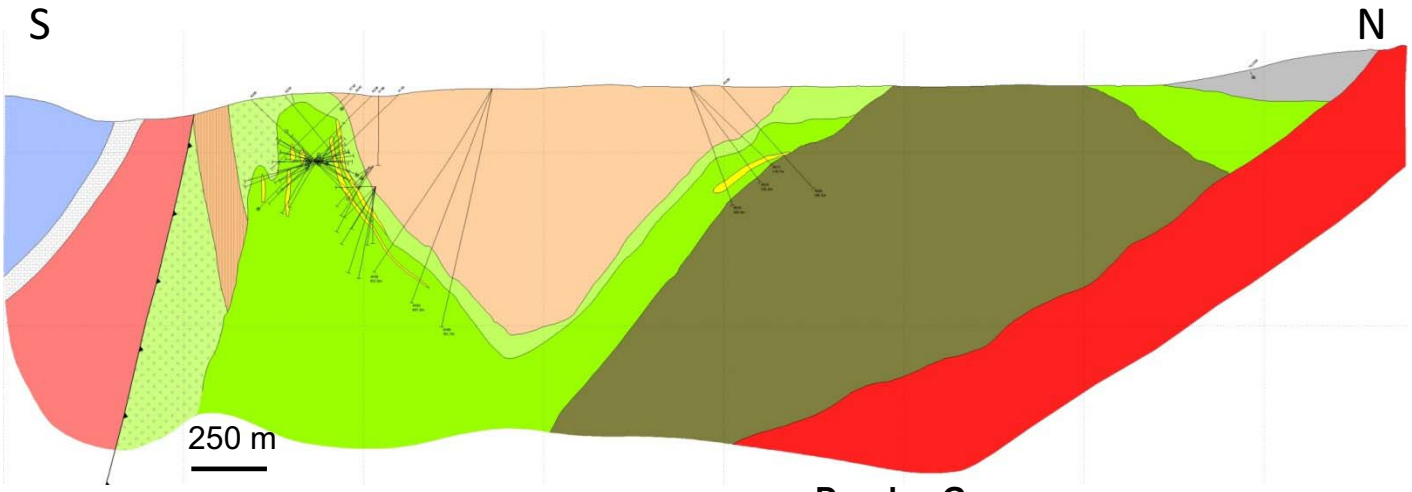

Devonian Heemskirk granite

Devonian siliciclastic sandstone & siltstone

Silurian siliciclastic sandstone, siltstone

Ordovician siliciclastic conglomerate, siltstone

Crimson Creek Formation
Cambrian greywacke

Dundas Group,
Cambrian volcaniclastic conglomerate, sandstone

McIvor Hill complex, Cambrian

Serpentinized ultramafic, skarn

Mineralized zones

Gabbro

Oonah Formation

Proterozoic siliciclastic sandstone, siltstone

Fig. 1.

This is a preprint, the final version is subject to change, of the American Mineralogist (MSA)
Cite as Authors (Year) Title. American Mineralogist, in press.
(DOI will not work until issue is live.) DOI: http://dx.doi.org/10.2138/am-2016-5509

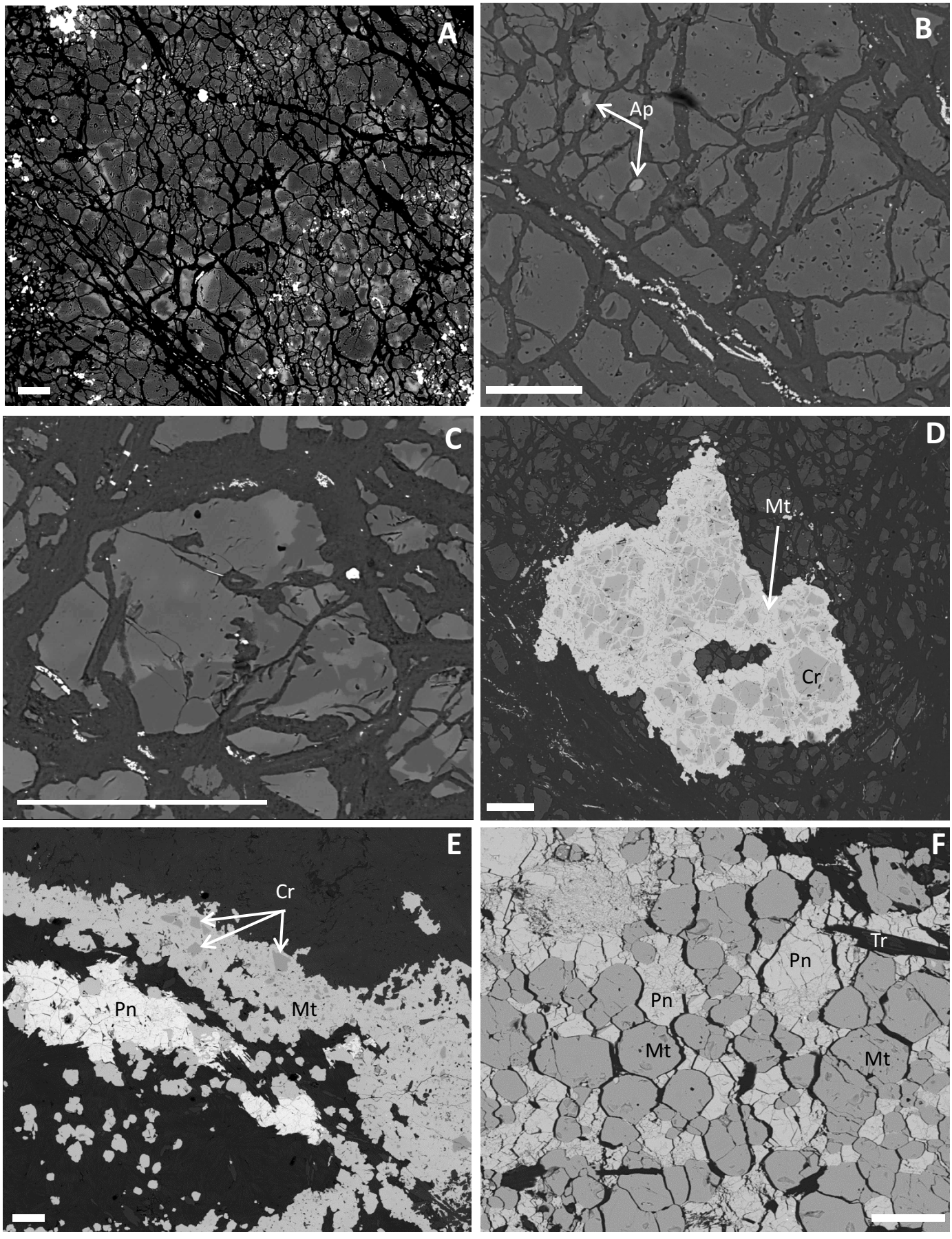

Fig. 2.

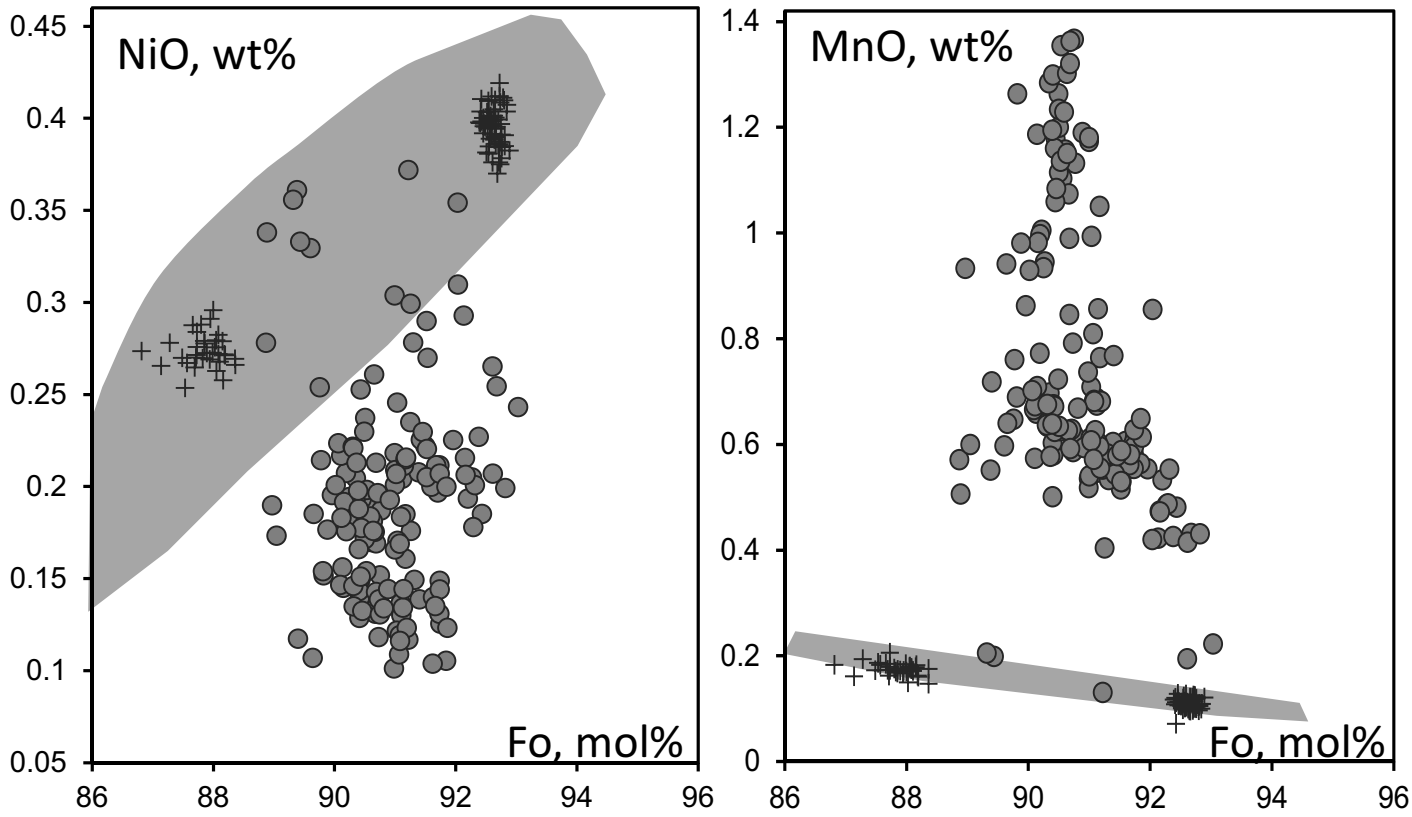
NiO, wt%
Fo, mol%
0.45
0.4
0.35
0.3
0.25
0.2
0.15
0.1
0.05
86
88
90
92
94
96
MnO, wt%
Fo, mol%
1.4
1.2
1
0.8
0.6
0.4
0.2
0

Fig. 3.

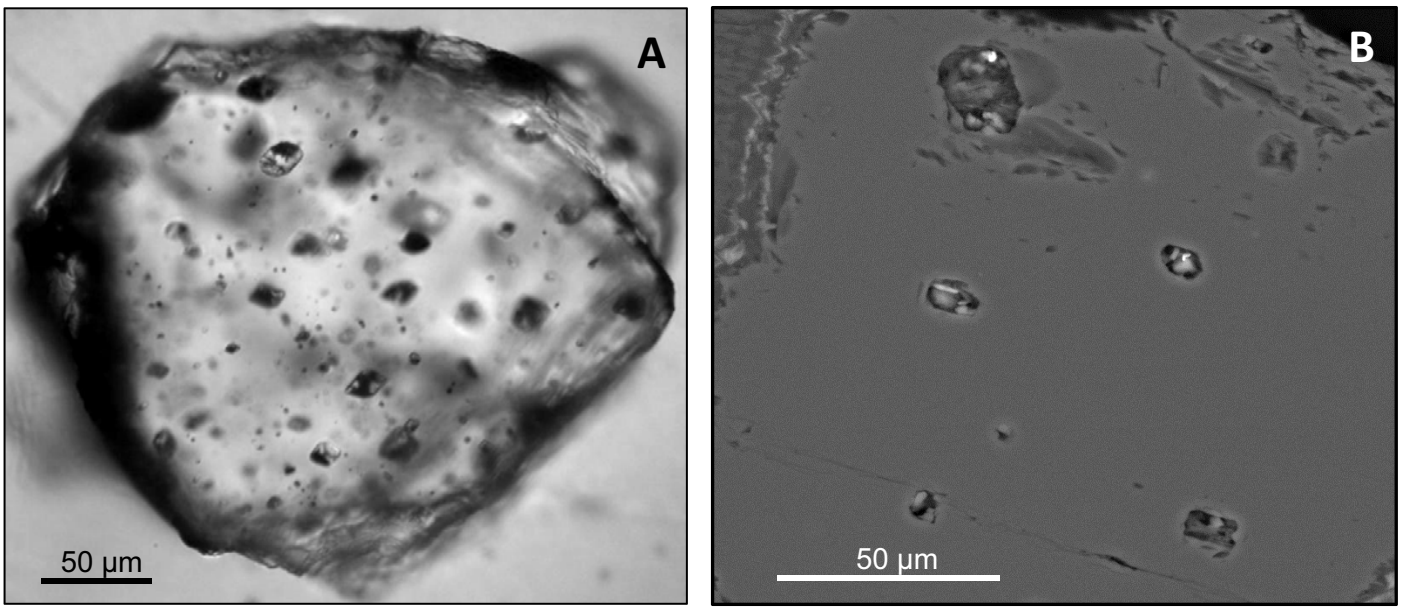
A
50 µm
B
50 µm

Fig. 4.

This is a preprint, the final version is subject to change, of the American Mineralogist (MSA)
Cite as Authors (Year) Title. American Mineralogist, in press.
(DOI will not work until issue is live.) DOI: http://dx.doi.org/10.2138/am-2016-5509

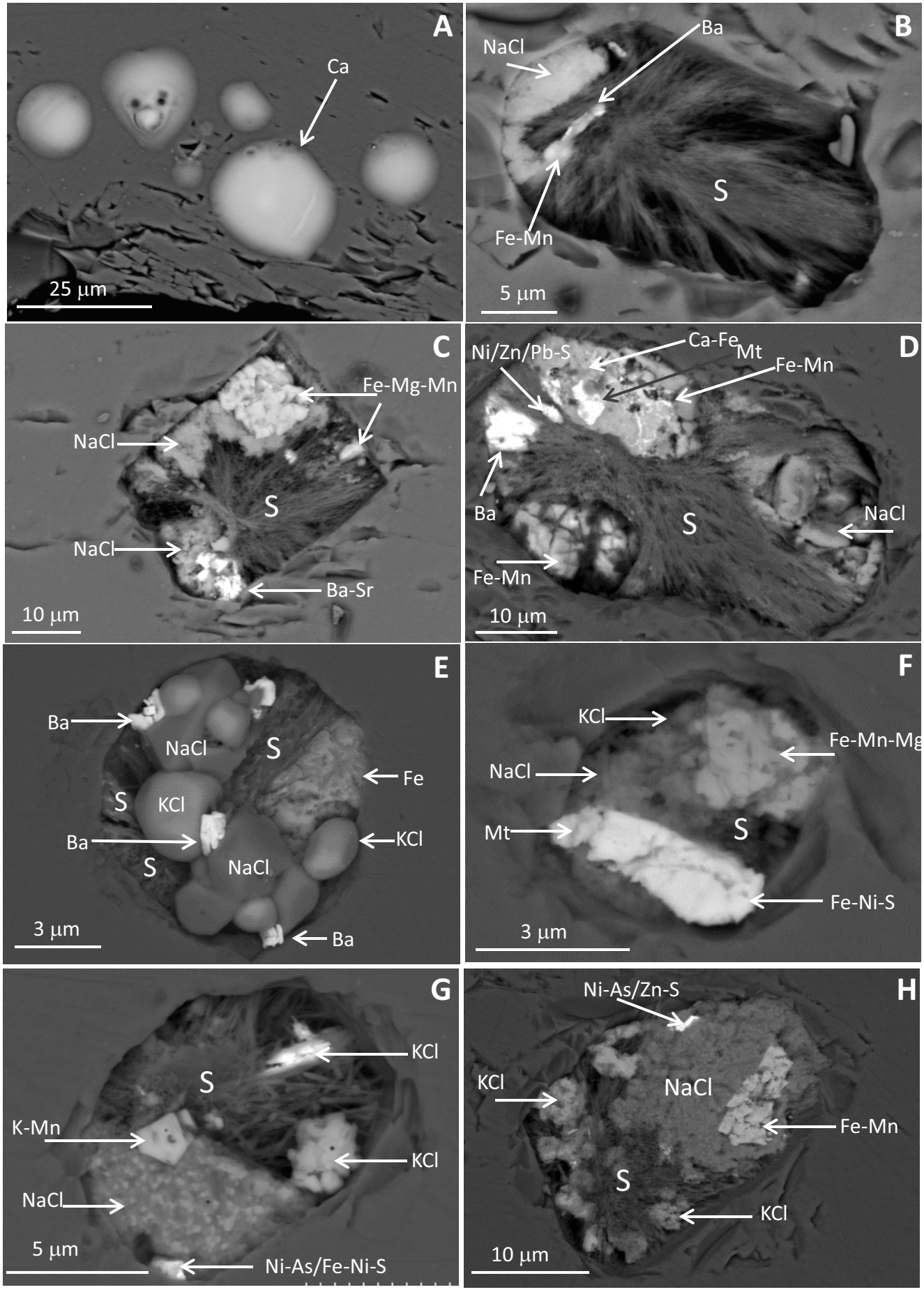

Fig. 5.

This is a preprint, the final version is subject to change, of the American Mineralogist (MSA)
Cite as Authors (Year) Title. American Mineralogist, in press.
(DOI will not work until issue is live.) DOI: http://dx.doi.org/10.2138/am-2016-5509

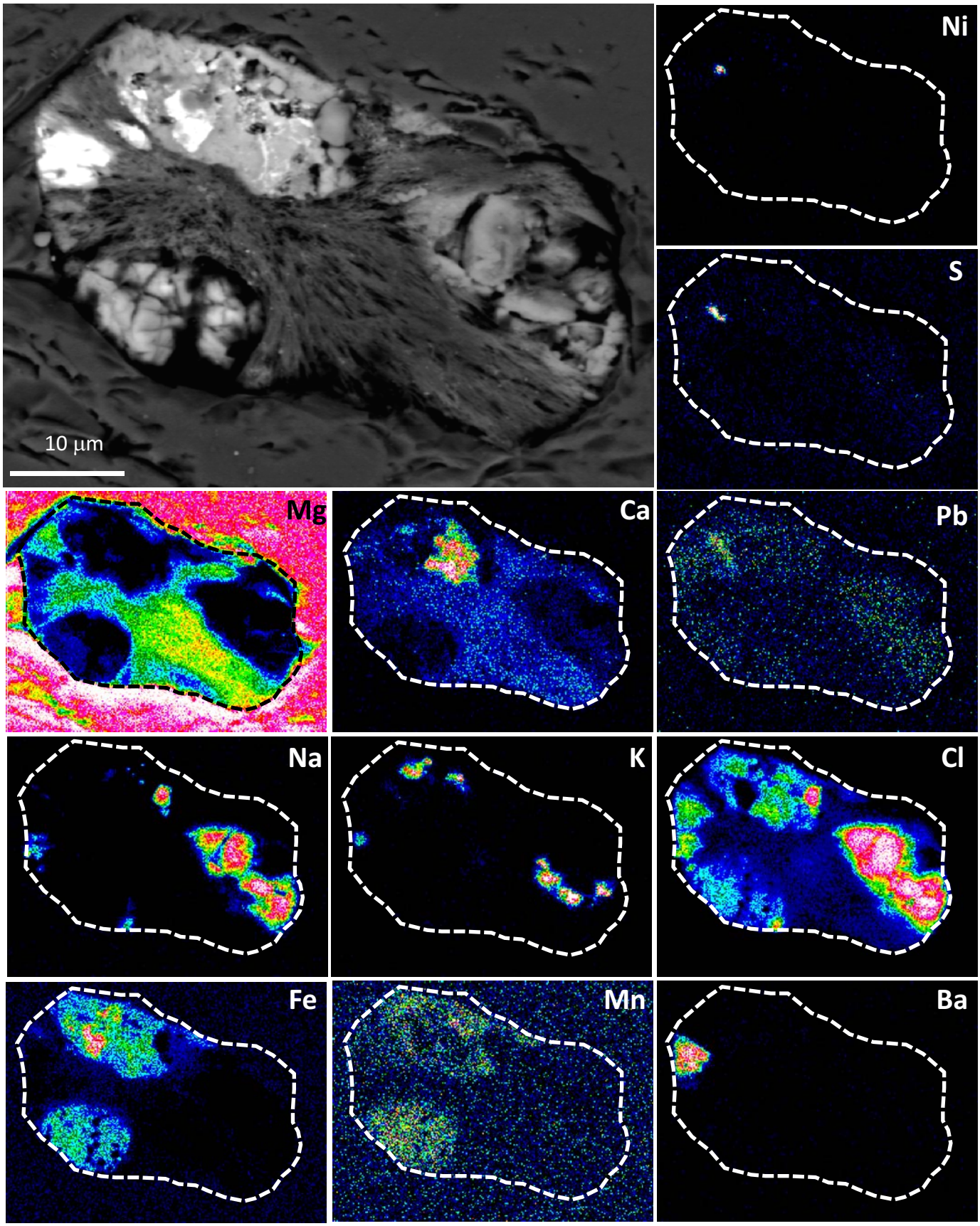

Fig. 6.

This is a preprint, the final version is subject to change, of the American Mineralogist (MSA)
Cite as Authors (Year) Title. American Mineralogist, in press.
(DOI will not work until issue is live.) DOI: http://dx.doi.org/10.2138/am-2016-5509

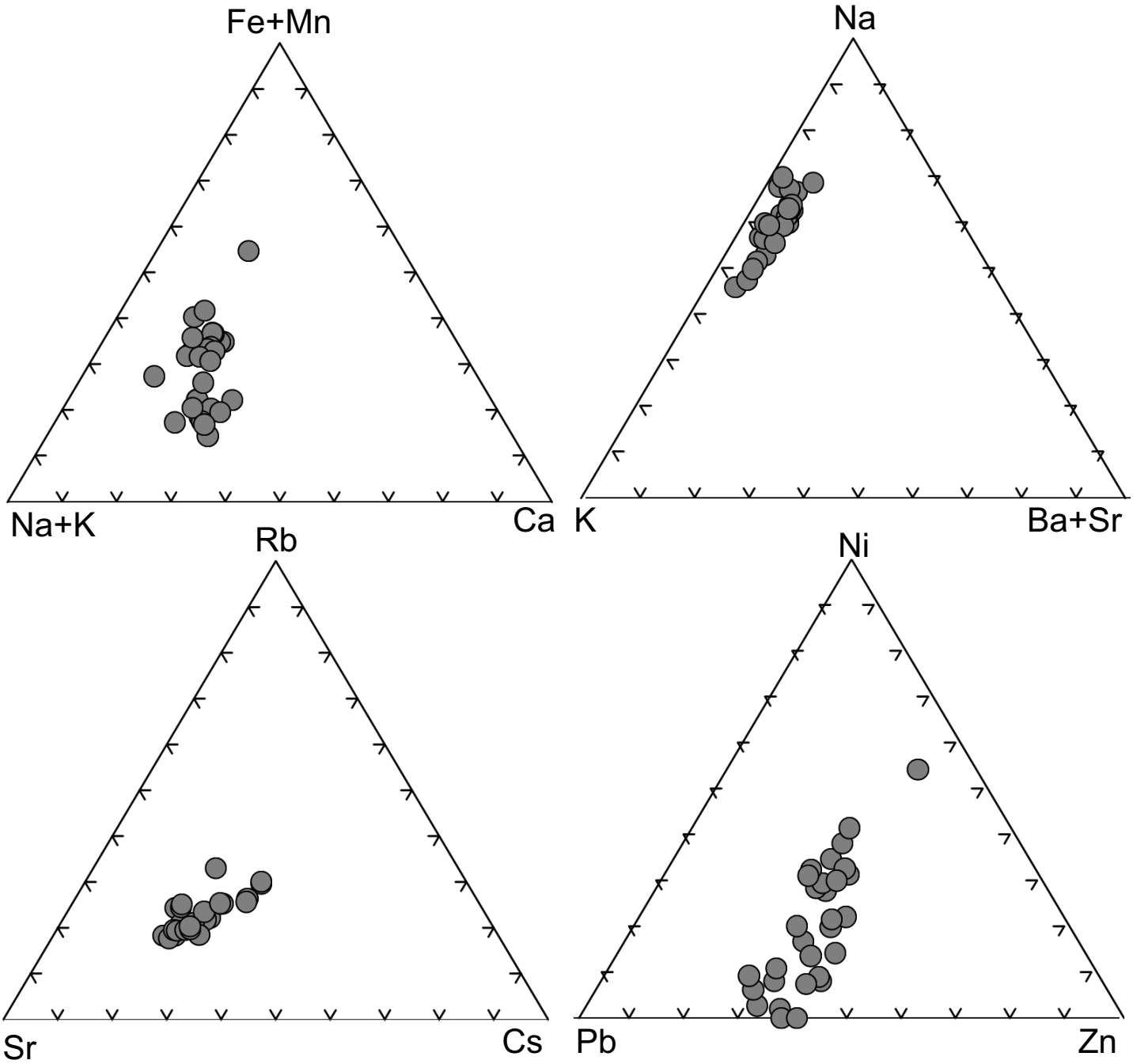

Fig. 7.

This is a preprint, the final version is subject to change, of the American Mineralogist (MSA)
Cite as Authors (Year) Title. American Mineralogist, in press.
(DOI will not work until issue is live.) DOI: http://dx.doi.org/10.2138/am-2016-5509

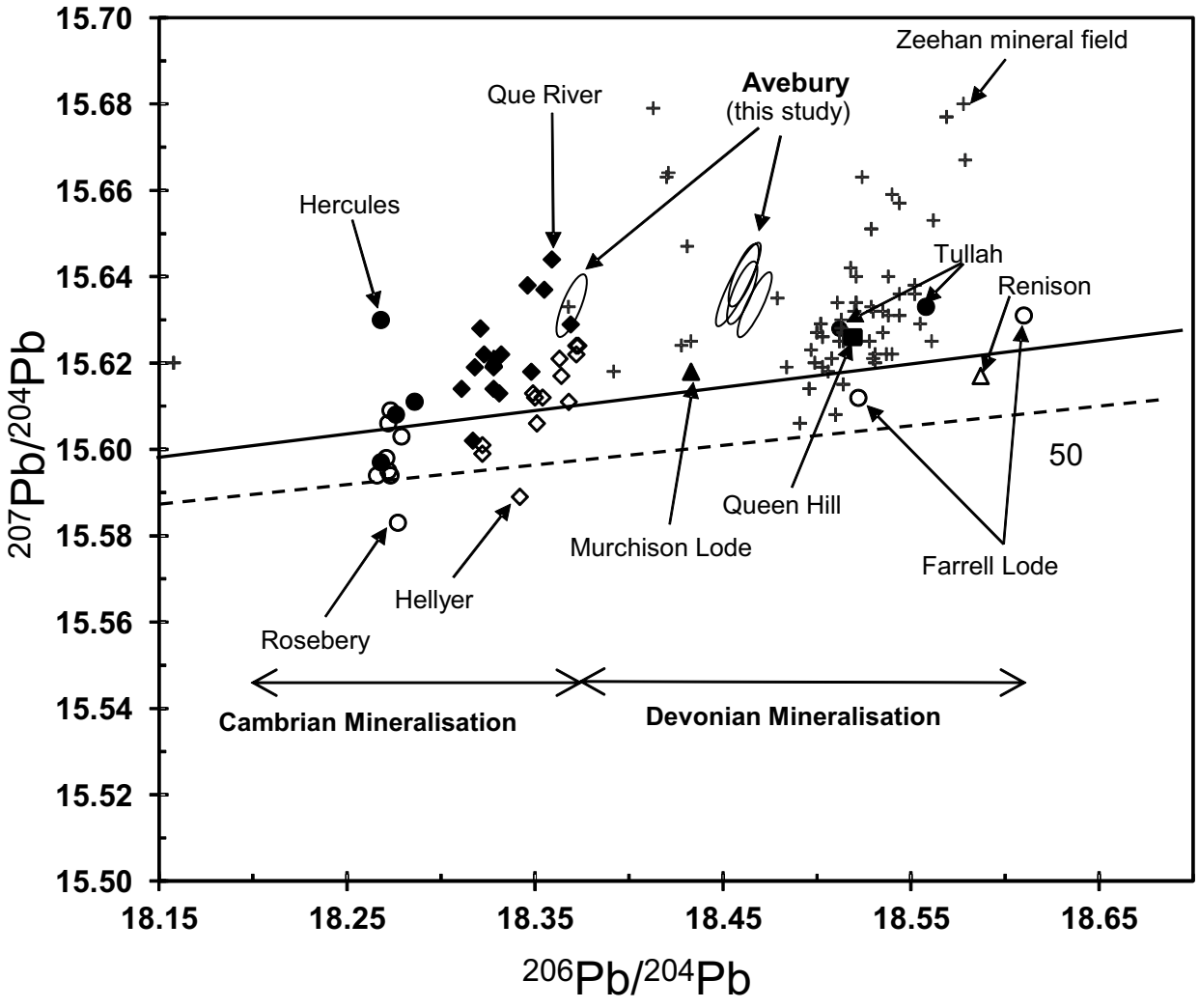

Fig. 8.

This is a preprint, the final version is subject to change, of the American Mineralogist (MSA)
Cite as Authors (Year) Title. American Mineralogist, in press.
(DOI will not work until issue is live.) DOI: http://dx.doi.org/10.2138/am-2016-5509

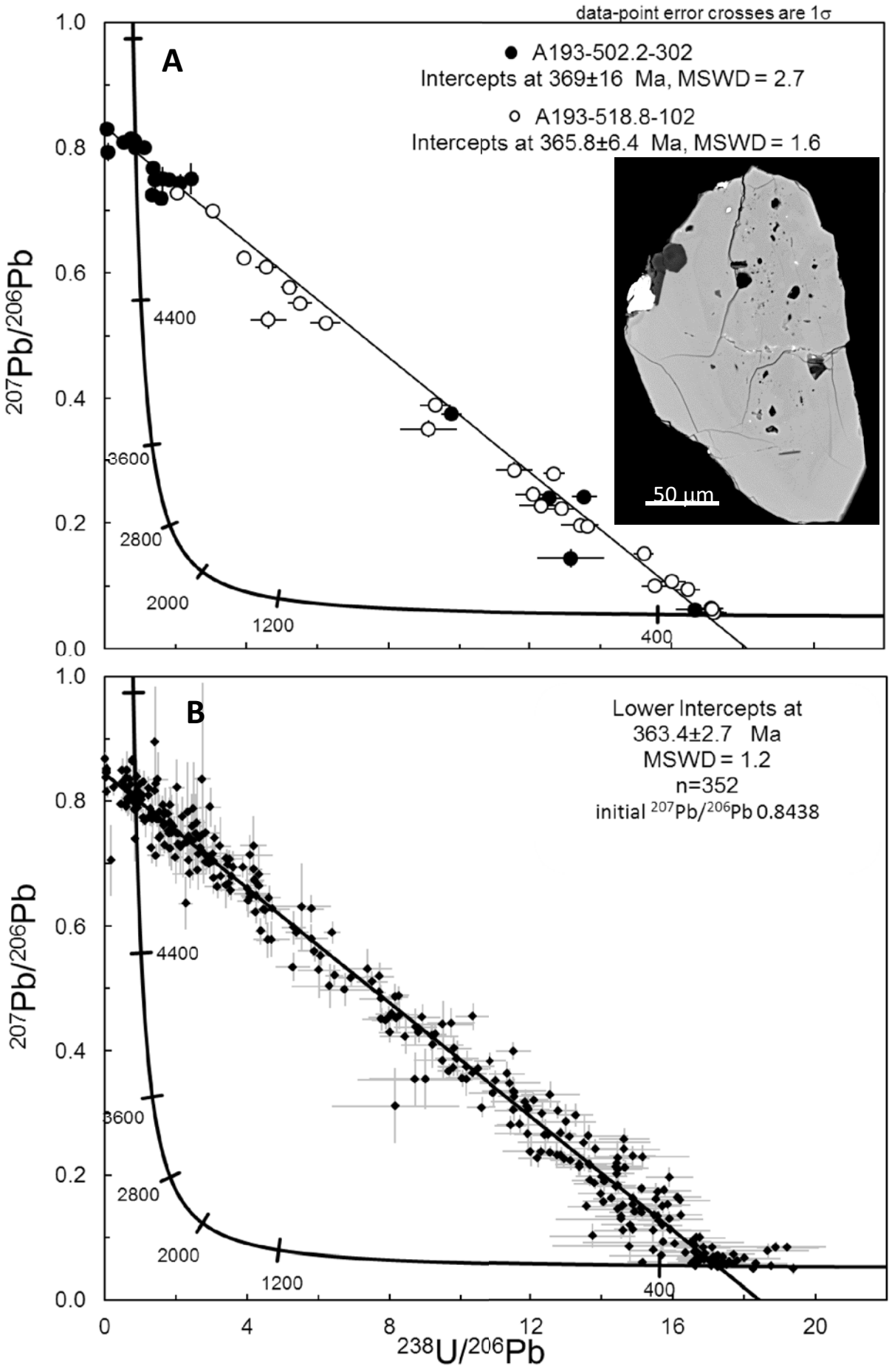

Fig. 9.

This is a preprint, the final version is subject to change, of the American Mineralogist (MSA)
Cite as Authors (Year) Title. American Mineralogist, in press.
(DOI will not work until issue is live.) DOI: http://dx.doi.org/10.2138/am-2016-5509

Table 1. Selected major and trace elements and Rb-Sr, Sm-Nd and U-Th-Pb isotope compositions of Avebury peridotites

	UO66-5	UO66-12	UO66-13	UO66-20	UO66-21
SiO_2	33.38	37.60	35.21	30.35	21.74
Al_2O_3	0.21	0.29	0.19	0.02	0.12
Fe_2O_3	14.30	14.26	16.36	20.78	39.67
MnO	0.31	0.30	0.26	0.37	0.34
MgO	38.24	34.88	35.41	35.77	26.72
CaO	0.10	1.75	0.29	0.01	<0.01
Cr_2O_3	0.25	0.40	0.28	0.15	0.17
NiO	0.38	0.26	0.70	0.67	2.36
S wt%	0.19	0.22	0.58	0.37	1.53
Rb ppm	0.064	1.467	1.830	0.064	0.151
Sr ppm	0.159	0.985	0.491	0.252	0.478
$^{87}Rb/^{86}Sr$	1.160	4.322	10.86	0.735	0.913
$^{87}Sr/^{86}Sr$	0.72607±2	0.74105±2	0.77380±2	0.72317±2	0.72358±2
Sm ppm	0.037	0.174	0.073	0.013	0.010
Nd ppm	0.107	0.519	0.216	0.039	0.032
$^{147}Sm/^{144}Nd$	0.2070	0.2024	0.2043	0.2053	0.1892
$^{143}Nd/^{144}Nd$	0.512452±8	0.512461±7	0.512493±6	0.512494±28	0.512482±17
ε_{Nd} now	-3.5	-3.3	-2.7	-2.7	-2.9
U ppm	0.231	0.419	0.347	0.185	0.309
Th ppm	0.089	0.150	0.102	0.058	0.082
Pb ppm	5.6	4.4	8.7	4.5	32.0
$^{238}U/^{204}Pb$	2.63	6.07	2.54	2.62	.61
$^{232}Th/^{204}Pb$	1.05	2.25	0.77	0.85	0.7
$^{206}Pb/^{204}Pb$	18.607	18.708	18.603	18.612	18.490
$^{207}Pb/^{204}Pb$	15.644	15.652	15.648	15.642	15.638
$^{208}Pb/^{204}Pb$	38.418	38.436	38.433	38.399	38.390
$^{87}Sr/^{86}Sr(i)$	0.72028	0.71947	0.71958	0.71950	0.71902
ε_{Nd} (i)	-4.0	-3.6	-3.1	-3.1	-2.6
$^{206}Pb/^{204}Pb(i)$	18.46	18.36	18.46	18.46	18.45
$^{207}Pb/^{204}Pb(i)$	15.64	15.63	15.64	15.63	15.64
$^{208}Pb/^{204}Pb(i)$	38.40	38.40	38.42	38.38	38.39

Rb-Sr and Sm-Nd results corrected for blank (0.1ng Sr, Rb/Sr=0.3, $^{87}Sr/^{86}Sr$=0.715, 0.1 ng Nd, Sm/Nd=0.16, $^{143}Nd/^{144}Nd$=0.5115). Uncertainties given for present-day (blank-corrected) $^{87}Sr/^{86}Sr$ and $^{143}Nd/^{144}Nd$ are measured 2se. Age-corrected isotope ratios (i) are calculated at 357 Ma.